In Situ Carbon-Coated Yolk–Shell V$_2$O$_3$ Microspheres for Lithium-Ion Batteries

Le Jiang, Yang Qu, Zhiyu Ren, Peng Yu, Dongdong Zhao, Wei Zhou, Lei Wang, and Honggang Fu*

Key Laboratory of Functional Inorganic Material Chemistry, Ministry of Education of the People's Republic of China, Heilongjiang University, Harbin 150080, P. R. China

S *Supporting Information*

ABSTRACT: Metal oxide-based materials with yolk–shell morphology have been intensively investigated as important anodes for Li-ion batteries due to their large ion storage ability, high safety, and excellent cycling stability. In this work, *in situ* carbon-coated yolk–shell V$_2$O$_3$ microspheres were synthesized via a template-free polyol solvothermal method. The growth of yolk–shell microspheres underwent coordination and polymerization, followed by an inside–out Ostwald-ripening process and further calcination in N$_2$ atmosphere. The thin amorphous carbon layers coating on the microspheres' surface came from polyol frameworks which could protect V$_2$O$_3$ during the charge–discharge process and led to a better stability in Li-ion batteries. The *in situ* carbon-coated yolk–shell V$_2$O$_3$ microspheres showed a capacity of 437.5 mAh·g^{-1} after 100 cycles at a current density of 0.1 A·g^{-1}, which was 92.6% of its initial capability (472.5 mAh·g^{-1}). They were regarded as excellent electrode materials for lithium-ion batteries and exhibit good electrochemistry performance and stability.

KEYWORDS: *yolk–shell, vanadium oxide, microsphere, in-situ carbon coating, Li-ion battery*
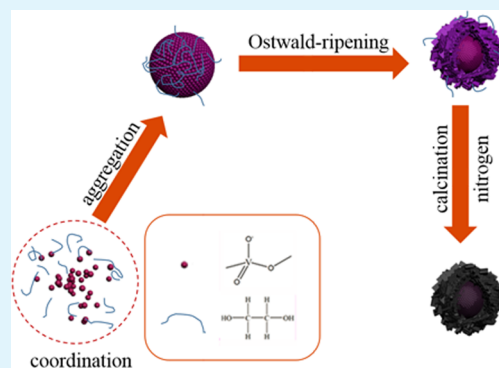
■ INTRODUCTION

Lithium-ion batteries (LIBs) have been focused on their combination of high energy density and power density, as a key component of energy storage with good electrochemical reversibility, cyclic stability, high conversion efficiency, and no gaseous exhaust.[1−3] However, the electrochemical performance of LIBs strongly depends on the electrode properties including anodes and cathodes, not only the materials themselves but also the surface/interface effect. Seeking suitable anode materials with low cost, stability, and full of excellent surface/interface properties is a pressing objective. The conventional LIBs use carbon-based materials (typically graphite) as anode materials, which have the advantages of low cost, high abundance, and outstanding kinetics.[4] Nevertheless, there are two disadvantages that greatly limit their practical applications for large-sized batteries.[4−8] One is the volume expansion and shrinkage of carbon materials during Li-ion intercalation and deintercalation that fatigue the graphite particles, causing cracking, leading to a loss in electrical contact between the resulting particles, and thereby decreasing capacity, and the other limitation comes from the safety concerns arising from lithium dendrite formation during the overcharge process owing to a low Li-intercalation potential of the graphite anode approaching 0 V (vs Li/Li$^+$). Recently, metal oxides shown as alternatives to carbon-based materials with good safety and cycling stability, such as Li$_4$Ti$_5$O$_{12}$, have been utilized for anode materials. Although they have shown perfect stability, the low specific capacity could not satisfy their industrial applications.[9]

Vanadium sesquioxides (V$_2$O$_3$), as common functional vanadium oxides, have been studied as high capacity materials for LIBs on account of their natural abundance, better safety than currently used materials, and low toxicity for lithium-ion storage.[10] So far a number of V$_2$O$_3$, and even one-dimensional carbon/V$_2$O$_3$ materials, were prepared by different methods and showed outstanding capacity and stability as anode materials.[11−14] The present works about V$_2$O$_3$ nanostructure materials could be summarized as follows:[15,16] (1) the preparing process is complex and fussy, (2) template or surfactant should be used to control the morphologies, (3) pure phase yolk–shell microsphere nanostructure is rare. However, compared with the low surface area of one-dimensional materials, yolk–shell nanostructure materials with high surface area, low density, and high loading capacity are gradually capturing more and more attention since they have emerged at the frontier between materials chemistry and many other fields, such as electronics, biomedical, pharmaceutical, optics, and catalysis.[17−19] So far, great deals of yolk–shell semiconductors have been fabricated and represented outstanding properties in dye-sensitized solar cells, photocatalysis, drug delivery, gas sensors, and LIBs.[20−23] Yolk–shell semiconductors could be excellent electrode materials in LIBs for the following reasons: (i) a large electrode/electrolyte contact area and short path

lengths for Li$^+$ and electronic transport, leading to high charge–discharge rates and (ii) easy accommodation of the strain of lithium-ion intercalation/deintercalation, improving the recharge ability of the batteries. Thus, we have reasons to believe that yolk–shell V$_2$O$_3$ materials possess an outstanding surface/interface effect and excellent physicochemical properties that would play an important role for LIBs. Furthermore, carbon coating is one of the most widely used surface modification techniques for LIB materials, and it could also be used for anode materials since they may serve as perfect barriers to protect the inner active materials and maintain their high capacities.[24,25]

On the basis of the considerations above, carbon-coating yolk–shell V$_2$O$_3$ microspheres are synthesized via a polylol solvothermal route by using ethylene glycol (EG) without any surfactant and further calcinations under nitrogen atmosphere. EG is recognized as a structure-directing agent, ligand, as well as a pore-making agent and carbon resource for the formation of yolk–shell microspheres.[26,27] The reducibility of EG and the reducing gas from pyrolysis of the EG framework perfectly protect the stability of V^{3+} during the preparation of the V$_2$O$_3$ microspheres. It is notable that the carbon of the EG framework is reserved when calcinations under nitrogen atmosphere and *in situ* coating on the surface of V$_2$O$_3$ nanoparticles form thin carbon layers. Moreover, lots of pores are formed when pyrolysis by the gas etching and framework shrink. The *in situ* carbon-coated yolk–shell V$_2$O$_3$ microspheres are utilized as electrode materials for LIBs and exhibit good electrochemical performance owing to the abundant surface/interface space and pores of yolk–shell structures which favor lithium intercalation/deintercalation as well as the stability and high specific capacity of V$_2$O$_3$.

EXPERIMENTAL PROCEDURES

Synthesis of *in Situ* Carbon-Coated Yolk–Shell Vanadium Oxide Microspheres. A typical synthesis of yolk–shell vanadium oxide microspheres is as follows. All of the chemicals were analytical-grade and used without further purification. An amount of 1.17 g (0.01 mol) of ammonium metavanadate is dissolved in 40 mL of EG by magnetic stirring to form a clear yellow solution. Then the solution was transferred into a 50 mL Teflon-lined stainless-steel autoclave, which was then sealed and heated at 180 °C for suitable times. After the solvothermal reaction, purple precipitation (vanadium–EG glycolate precursor) was obtained. The precursor was purified by three centrifugation and redispersion cycles with absolute ethyl alcohol and dried under vacuum at 60 °C for 4 h. The carbon-coated yolk–shell V$_2$O$_3$ microspheres were prepared by calcining the precursor in N$_2$ at 500 °C for 2 h.

Characterization. X-ray powder diffraction (XRD) patterns were obtained by Bruker D8. Scanning electron microscopy (SEM) micrographs were taken using a Hitachi S-4800 instrument operating at 15 kV. The transmission electron microscopy (TEM) experiment was performed on a JEM-2100 electron microscope (JEOL, Japan) with an acceleration voltage of 200 kV. Carbon-coated copper grids were used as the sample holders. Raman measurements were performed with a JobinYvon HR 800 micro-Raman spectrometer at 457.9 nm. The laser beam was focused with a 50× objective lens to an ca. 1 μm spot on the surface of the sample. The pyrolysis experiments of vanadium–EG precursor were carried out in TG (TA, Q600) under a stream of air at a heating rate of 10 °C·min^{-1}. The specific surface area was determined according to the Brunauer–Emmett–Teller (BET) method using a Tristar II 3020 surface area and porosity analyzer (micromeritics). The X-ray photoelectron spectra (XPS) were examined by using a Kratos-AXIS ULTRA DLD apparatus with Al(Mono) X-ray source, and the binding energies were calibrated with respect to the signal for adventitious carbon (binding energy = 284.6

eV). The electrochemical measurements were performed at ambient temperature. The electrochemical properties of the yolk–shell V$_2$O$_3$ microspheres for LIBs were investigated by using the as-prepared model test cells. The V$_2$O$_3$ yolk–shell microsphere anode was tested in a half-cell configuration using Li metal as the standard cathode. Test electrodes were prepared by pasting a mixture of 80 wt % active materials, 10 wt % super-P carbon black, and 10 wt % poly inylidene fluorides (PVDF) mixed into *N*-methyl-2-pyrrolidinone (NMP). The obtained slurry was cast onto a copper foil and dried in vacuum at 110 °C for 10 h to remove excess solvent and cut to Φ14 mm sheets, pressed at 3 MPa. The active materials loaded on the electrode were about 1.0–1.5 mg·cm^{-2}. CR2025 coin cells were assembled in an argon-filled glovebox. Electrochemical measurements were carried out on coin-type cells with lithium metal as the counter/reference electrode and the Celgard 2400 membrane as the separator. The electrolyte solution was obtained by dissolving 1 M LiPF$_6$ into a mixture of ethylene carbonate (EC) and dimethyl carbonate (DMC) (EC/DMC, 50:50 w/w). Charge–discharge cycles of the half-cells were evaluated between 0.1 and 3 V vs Li$^+$/Li at room temperature using a LAND CT2001A model battery test system (Wuhan Jinnuo Electronics, Ltd.) under constant current conditions. The charge–discharge capacities of the yolk–shell V$_2$O$_3$ microspheres were calculated according to the weight of the active material in the electrode.

RESULTS AND DISCUSSION

Ethylene glycol (EG) possesses strong coordination ability due to the two hydroxyl groups as bidentate ligands. For the reasons above, EG was used as a structure-directing agent to synthesize different oxides with interesting morphologies, such as nanorods, nanospheres, and so on.[28–30] In this work, EG is utilized as a structure-directing agent to prepare V$_2$O$_3$ nanospheres. The time-dependent morphology evolution of the vanadium glycolate yolk–shell precursor is studied by SEM. As shown in Figure 1A, the morphology of the samples is
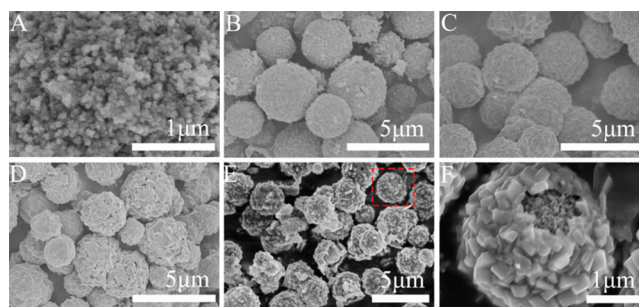
Figure 1. SEM images of time-dependent morphology evolution of the vanadium glycolate yolk–shell precursor. (A: 5 min, B: 30 min, C: 1 h, D: 5 h, E: 12 h, and F: magnifying yolk–shell microsphere in E).

nanoparticles after 5 min solvothermal reaction at 180 °C. Uniform microspheres with diameter of approximately 1–2 μm are formed after 30 min. An interesting phenomenon which can be learned from Figure 1B–D is that many cubes are present on the surface of the microspheres, and the small cubes congregate more and more and grow larger along with the prolonging of the reaction times from 1 to 5 h. After 12 h solvothermal reaction, yolk–shell microspheres with a diameter of 2–3 μm are prepared. The high magnification SEM image in Figure 1F clearly shows the yolk–shell structure with a loose and porous yolk and cubic aggregate shell. TEM images of microspheres at different reaction time in Figure S1 (Supporting Information) clearly indicate the inside-out Ostwald-ripening process from solid to yolk–shell structure.

XRD patterns in Figure S2 (Supporting Information) investigate the crystalline phase evolution of different reaction times. It can be observed that the product changes from the amorphous state to crystallization, and after 1 h, the obvious changes can be seen, implying the crystalline phase changes. The typical crystalline phase of the V—EG glycolate precursor is difficult to be attributed but very similar to other metal—EG precursors.[31−33] The FT-IR and Raman curves (see Figures S3A and S4, Supporting Information) indicate the V—EG glycolate framework as well.

The V_2O_3 yolk—shell microsphere with *in situ* carbon-coating layer could be easily prepared by annealing the vanadium glycolate precursor under N_2 atmosphere. Importantly, the V_2O_5 yolk—shell microsphere would be obtained if the precursor was annealed in air because the multivalent V ion may change to the highest valence state (V^{5+}) with the help of oxygen. Before calcinations, the TG curve is studied to determine the annealing temperature under N_2 atmosphere. The TG curve of the glycolate precursor in Figure S5A (Supporting Information) indicates that 500 °C is the optimal annealing temperature because there is no obvious weight loss after 500 °C. Thus, in order to conserve energy, 500 °C is chosen to prepare the V_2O_3 yolk—shell microsphere. After being calcined, surface functional groups of yolk—shell microsphere precursors disappear (Figure S3B, Supporting Information) and the carbon layer forms on the sample surface. To certify the existence of the carbon layer, the TG curve under air atmosphere of the calcined sample is shown in Figure S5B (Supporting Information), in which carbon loss could be seen.

On the basis of the above characterization, the formation process of the yolk—shell vanadium glycolate microsphere could be depicted as shown in Scheme 1. First, a rough

Scheme 1. Scheme of the Formation Process of the Yolk—Shell V_2O_3 Microsphere
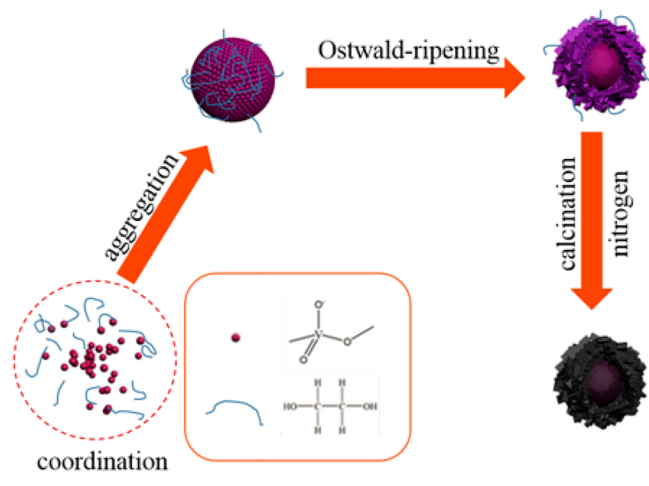
vanadium glycolate microsphere is formed by the coordination of the vanadium ion with EG, and the reason for polymerization of nanoparticles may be the hydrogen bond and van der Waals interaction. This could be learned as an assembling process from the nanoparticles to the microspheres. Second, while reaction time is lengthening, cubes coated on the microsphere become more and more. This is considered as an inside-out Ostwald-ripening process, which commonly refers to the growth of the outer crystalline shell of the solid particles by the consumption and recrystallization of the interior materi-

al.[34,35] Finally, the formation of the shell could possibly be associated with the relatively large particle size of the microspheres and the poor solubility of vanadium oxide in the solvent. The dissolution process mainly takes place in the particular region under the surface layer, whereas the interior core remains mostly intact. The interior core is finally growing into a tight solid microsphere and leaves space between outside shells to form yolk—shell structure. The TEM images (Figure S1, Supporting Information) have certificated the inside-out Ostwald-ripening process as well. Then, after the precursor is calcined in N_2 atmosphere, yolk—shell V_2O_3 microspheres with an *in situ* carbon-coated layer appears.

XPS in Figure 2 further demonstrates the formation of V_2O_3. High-resolution XPS illustrating the two peaks centered at 516.85 and 524.00 eV is attributed to the spin—orbit splitting of the components, V 2p3/2 and V 2p1/2, which are characteristic of vanadium in the +3 oxidation state, thus it indicates the preparation of V_2O_3.[36,37] Because the electronegativity of carbon is much bigger than that of vanadium, the O 1s core level at 530.1, 531.1, and 533.0 eV could be ascribed to the formation of V—O species, C—O species, and the adsorbed O_2, respectively.[38] C 1s core levels at 284.6, 285.5, and 288.8 eV are assigned to amorphous carbon, the formation of C—O species, and the adsorbed CO_2, respectively.

SEM images of V_2O_3 yolk—shell microsphere are shown in Figure 3. The prepared microsphere copies the precursor's morphology without any obvious change. The V_2O_3 yolk—shell microsphere with cubic aggregation shell is approximately 2—3 μm in diameter, which is observed from the high-resolution SEM in Figure 3C. In addition, pores could also be observed from the SEM images which may be caused by the gas from the pyrolysis of the glycolate precursor. The N_2 adsorption—desorption isotherms (Figure S6, Supporting Information) of the V_2O_3 yolk—shell microsphere exhibit a combined type IV sorption isotherm that gives evidence of the pores. The BET surface area of the V_2O_3 yolk—shell microsphere is 70.5 m^3/g. The high surface area is assigned to the yolk shell structure and the etching pores on the shell's surface. Thanks to the abundant pores, the Li ion could be easily flowing (intercalation/deintercalation). The XRD pattern of the yolk—shell microsphere precursors calcined in N_2 is shown in Figure 3D. It clearly shows that all the diffraction peaks of the sample calcined in N_2 match very well with the standard data from the rhombohedral crystalline phase V_2O_3 (JCPDS: 34-0187), indicating the formation of pure phase V_2O_3. In order to confirm the composition of the core, SEM and the energy-dispersive X-ray (EDX) linear scanning spectrum of a cut microsphere were done and shown in Figure S7 (Supporting Information) further indicating that although the morphology of the yolk and shell is a little different the composition of them is much more closed. In addition, two cavities between the yolk and shell could be seen from a SEM image in Figure S7A (Supporting Information). The content of V obviously declined at the two cavities, implying the yolk—shell structure which is in keeping with the SEM image. The change of O is not obvious because O exists everywhere in V_2O_3 and cavities with O_2 adsorption.

TEM and HRTEM images with different magnification in Figure 4 clearly represent the yolk—shell structure of the microsphere. It could be seen that the inner core is approximately 600 nm in diameter. The HRTEM images in Figure 4C and D display the lattice fringes with interlayer distances of 0.248 nm, which are related to the spacing of the
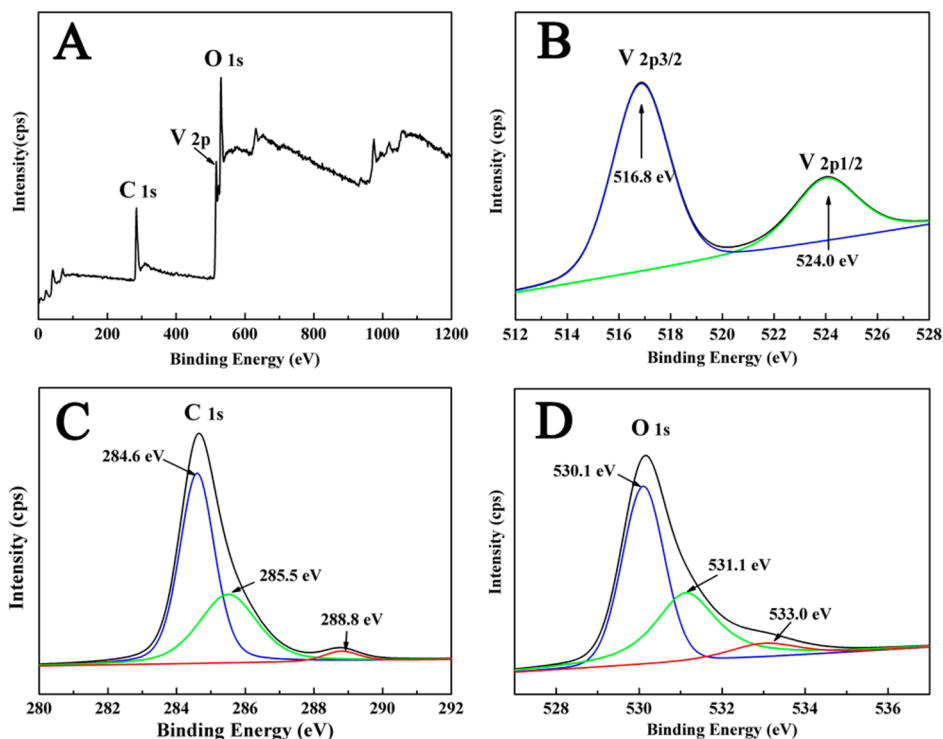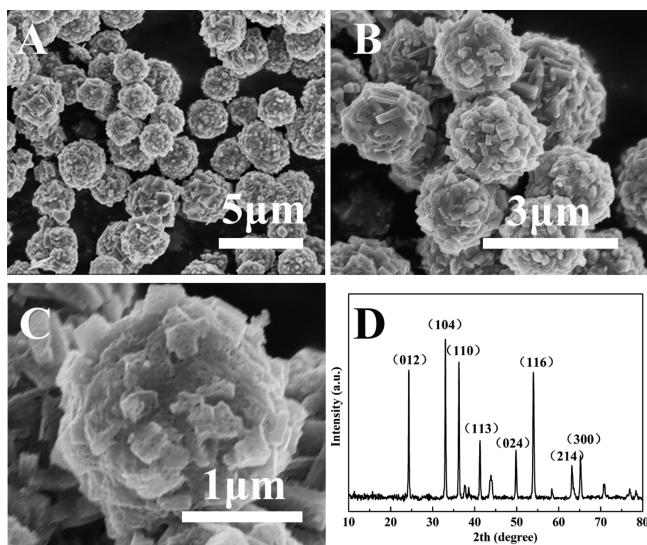
Figure 2. XPS of V_2O_3 the yolk−shell microsphere.

Figure 3. SEM images (A, B, C) and XRD spectra (D) of V_2O_3 yolk−shell microspheres.

Figure 4. TEM and HRTEM images of V_2O_3 yolk−shell microspheres (B and C are different parts of A, and D is the designated part of B).

(110) planes of the rhombohedral crystalline phase. Moreover, a very thin amorphous carbon layer (∼1−2 nm) can be observed from a high-resolution TEM image which is shown in Figure 4. These amorphous carbon layers are produced by the EG framework in the precursor and carbonized when calcined in N_2. The result is consistent with XPS spectra (Figure 2). However, the carbon layers coated on the surface of V_2O_3 microspheres protect them from corrosion and oxidation in order to make them stable. This can be proven by the XRD pattern in Figure S8 (Supporting Information), which illustrates that the carbon-coated V_2O_3 microspheres could retain the V_2O_3 phase after exposure in air for one year. The stable crystal
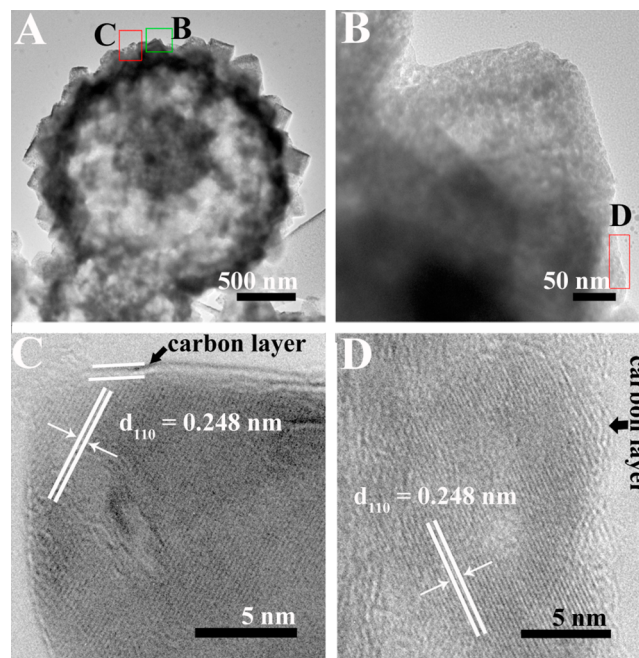
phase of V_2O_3 microspheres is very important to the electrochemical performance.

The V_2O_3 yolk−shell microsphere is a candidate anode material for LIBs because it possesses not only the proper electrode potential but also unique meso- and microscopic features. Such structural and morphological characteristics increase the interface between electrode and electrolyte and decrease the lithium ion diffusion distance, both of which are key optimal factors. Besides the above factors, the effects of
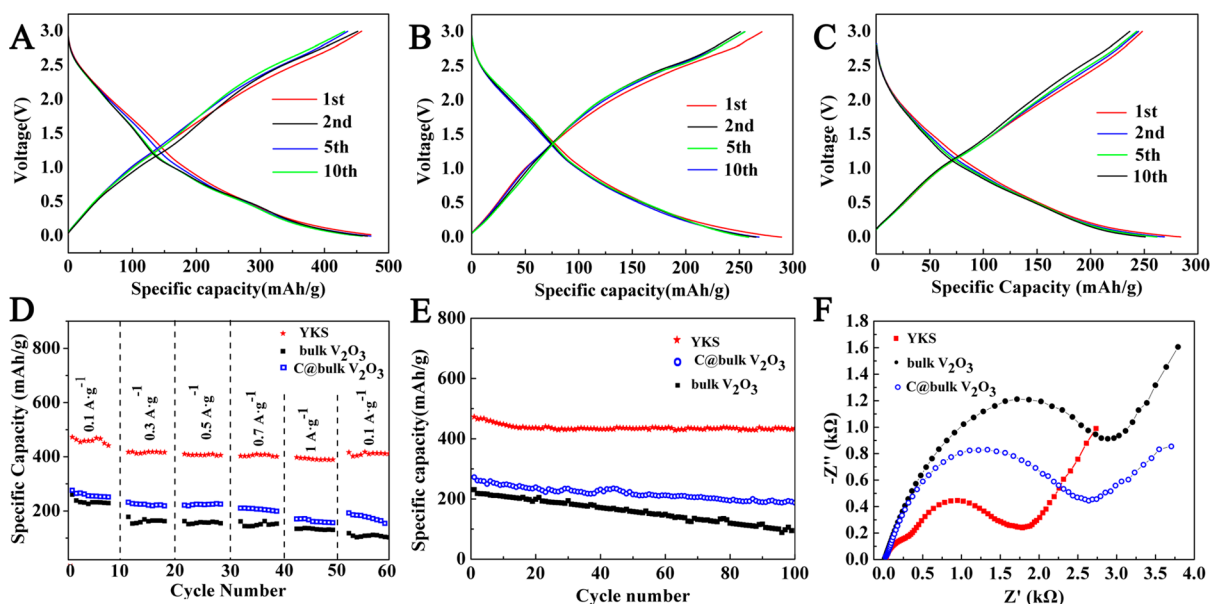
Figure 5. Charge/discharge profiles of V_2O_3 yolk−shell microsphere (YKS) (A), bulk V_2O_3 (B), and carbon-coated bulk V_2O_3 (C) at a current density of 100 mA·g^{-1}. (D) Rate capability of YKS, C@bulk V_2O_3 at various current densities between 0.1 and 1 A·g^{-1}. (E) Comparison of the cycling performance of YKS, bulk V_2O_3, and C@bulk V_2O_3 at 100 mA·g^{-1}. (F) Impedance plots of YKS, bulk V_2O_3, and C@bulk V_2O_3 electrodes.

annealing temperature which could cause the phase transformation and morphology are also crucial to electrochemical performance. The first discharge curves at a current density of 100 mA·g^{-1} of yolk−shell V_2O_3 microspheres annealed at different temperatures in Figure S10 (Supporting Information) demonstrated that the sample annealed at 500 °C possessed the best electrochemistry performance. The XRD patterns of these samples in Figure S11 (Supporting Information) further indicates that the original bixbyite phase changed to the rhombohedral phase at 500 °C, implying the rhombohedral phase favors the electrochemistry performance. Although the rhombohedral phase after 600 °C calcinations is not changed, the electrochemical performance is lower, which could be attributed to the growth of particles after calcination. Thus, 500 °C is the optimal annealing temperature in this work. Figure 5A, B, and C reveals the charge−discharge curves plotted as voltage vs specific capacity of the V_2O_3 yolk−shell microsphere annealed at 500 °C (YKS), bulk V_2O_3, and carbon-coated bulk V_2O_3 (synthesized method see Supporting Information) cells (for reference) in the voltage window of 0−3 V at a current of 100 mA·g^{-1}. On the first discharge, the discharge capacity of YKS is 472.5 mAh·g^{-1}, much higher than the bulk V_2O_3 and carbon-coated bulk V_2O_3 (C@ bulk V_2O_3). The charge curve profiles of YKS are similar to those earlier reported results that the V_2O_3 is reduced to lower valence state, most likely V^{2+} on the first discharge. The two short gentle slopes in the voltage range of 1.1 and 2.1 V most likely corresponded to the multistep oxidation of V^{2+} to higher valence states.[39] The CV curve in Figure S12 (Supporting Information) shows the two oxidation peaks at 1.3 and 2.6 V and reduction peaks at 0.6 and 1.1 V which could be attributed to the multistep oxidation of V^{3+} to higher valence states and V^{5+} reduced to lower valence states. These are well matched with the short gentle slope voltage value in the charge−discharge curves. On the other hand, the average delithiation voltage of YKS is above 1 V (versus Li/Li+), which is safe and facilitates weakening of the formation of the solid electrolyte interphase. Nevertheless, the initial capacity loss may result from irreversible lithium loss

which is due to the formation of a solid electrolyte interphase layer. The rate capability of the YKS at rates from 0.1 to 1 A·g^{-1} is shown in Figure 5D. In the initial period, YKS keeps a higher reversible capacity than the bulk one after the 10th cycle at a current density of 100 mA·g^{-1}. Even at a high current density of 1 A·g^{-1}, this material can still present a reversible capacity of 361.8 mAh·g^{-1}, indicating that the anode composed of YKS delivered a high rate performance. Moreover, the capacity can be restored to its original state when the current density is returned to 100 mA·g^{-1}. The great electric performance could be attributed to the excellent charge transfer in the yolk−shell structures. Although the theoretical capacity of V_2O_3 is as high as 1070 mAh·g^{-1}, few previous reports have reached the theoretical value because of the crystallization, impurity, low conductivity, and so on.[12] However, the stability of LIB electrode material is as important as the capacity. Figure 5E shows the cycle performance of these anode materials at a current density of 100 mA·g^{-1} for 100 cycles. After 100 cycles, the YKS delivers a capacity of 437.5 mAh·g^{-1}, which is 92.6% of its initial capability. In comparison, the C@ bulk V_2O_3 anode shows a better cycling stability than the bulk V_2O_3. The result further instructs the large difference between the YKS and the bulk one, associating with the carbon cladding on the V_2O_3 yolk−shell microsphere surface which increased the stability of V_2O_3. Figure 5F shows the Nyquist profiles of YKS, bulk V_2O_3, and C@ bulk V_2O_3. It can be seen that the curve of the YKS electrode is composed of two semicircles at high frequencies which are related to the electrolyte resistance and charge transfer resistance and an inclined line in low-frequency regions which is due to the ion diffusion within the anode material.[40,41] In comparison, the bulk V_2O_3 and C@bulk V_2O_3 plots show only one large semicircle. The enlarged semicircle diameter indicates an increase of resistance for charge transfer at the bulk V_2O_3−electrolyte interface. Comparing with the higher resistive solid electrolyte interphase formation for the bulk V_2O_3 and C@ bulk V_2O_3, it suggests once again that the YKS can possess better electrochemical properties while it charge−discharges in LIBs.

CONCLUSIONS

In conclusion, the *in situ* carbon-coated V_2O_3 yolk−shell microsphere was successfully synthesized via the facile template-free polyol solvothermal method and further calcinations in N_2. The V_2O_3 yolk−shell microsphere electrode exhibited excellent lithium-ion battery electrochemical stability. The first discharge capacity was up to 472.5 mAh·g^{-1}. After 100 cycles, they showed a capacity of 437.5 mAh·g^{-1}, which was 92.6% of its initial capability. The high capacity suggested that the unique yolk−shell structure could not only facilitate the electrolyte transporting in the process of Li-ion intercalation and deintercalation but also accommodated large volume variation during electrode reaction. Furthermore, the *in situ* carbon layer effectively protected V_2O_3 yolk−shell microspheres during the period of electrode reaction. The special *in situ* carbon-coated V_2O_3 yolk−shell microspheres were potential anode materials for lithium-ion batteries.

ASSOCIATED CONTENT

Ⓢ Supporting Information

FT-IR curve, Raman, TG, N_2 adsorption−desorption isotherms, and so on. This material is available free of charge via the Internet at http://pubs.acs.org.

AUTHOR INFORMATION

Corresponding Author

*E-mail: fuhg@vip.sina.com. Tel.: +86 451 8660 4330. Fax: +86 451 8667 3647.

Notes

The authors declare no competing financial interest.

ACKNOWLEDGMENTS

REFERENCES

(1) Nam, K. T.; Kim, D. W.; Yoo, P. J.; Chiang, C. Y.; Meethong, N.; Hammond, P. T.; Chiang, Y. M.; Belcher, A. M. Virus-enabled Synthesis and Assembly of Nanowires for Lithium Ion Battery Electrodes. *Science* **2006**, *312*, 885−888.

(2) Poizot, P.; Laruelle, S.; Grugeon, S.; Dupont, L.; Tarascon, J. M. Nano-sized Transition-metal Oxides as Negative-electrode Materials for Lithium-ion Batteries. *Nature* **2000**, *407*, 496−499.

(3) Cheng, F.; Liang, J.; Tao, Z.; Chen, J. Functional Materials for Rechargeable Batteries. *Adv. Mater.* **2011**, *23*, 1695−1715.

(4) Reddy, M. V.; Subba Rao, G. V.; Chowdari, B. V. R. Metal Oxides and Oxysalts as Anode Materials for Li Ion Batteries. *Chem. Rev.* **2013**, *113*, 5364−5457.

(5) Choi, S. H.; Kang, Y. C. Ultrafast Synthesis of Yolk-Shell and Cubic NiO Nanopowders and Application in Lithium Ion Batteries. *ACS Appl. Mater. Interfaces* **2014**, *6*, 2312−2316.

(6) Liu, H.; Chen, S.; Wang, G.; Qiao, S. Z. Ordered Mesoporous Core/Shell SnO_2/C Nanocomposite as High-Capacity Anode Material for Lithium-Ion Batteries. *Chem.—Eur. J.* **2013**, *19*, 16897−16901.

(7) Liang, J.; Cai, Z.; Tian, Y. Deposition SnO_2/Nitrogen-Doped Graphene Nanocomposites on the Separator: A New Type of Flexible Electrode for Energy Storage Devices. *ACS Appl. Mater. Interfaces* **2013**, *5*, 12148−12155.

(8) Shi, W.; Rui, X.; Zhu, J.; Yan, Q. Design of Nanostructured Hybrid Materials Based on Carbon and Metal Oxides for Li Ion Batteries. *J. Phys. Chem. C* **2012**, *116*, 26685−26693.

(9) Zhu, G.; Wang, Y. G.; Xia, Y. Y. Ti-based Compounds as Anode Materials for Li-ion Batteries. *Energy Environ. Sci.* **2012**, *5*, 6652−6667.

(10) Sun, Y.; Jiang, S.; Bi, W.; Wu, C.; Xie, Y. Highly Ordered Lamellar V_2O_3-based Hybrid Nanorods towards Superior Aqueous Lithium-ion Battery Performance. *J. Power Sources* **2011**, *196*, 8644−8650.

(11) Pang, H.; Cheng, P.; Yang, H.; Lu, J.; Guo, C. X.; Ning, G.; Li, C. M. Template-free Bottom-up Synthesis of Yolk-shell Vanadium Oxide as High Performance Cathode for Lithium ion Batteries. *Chem. Commun.* **2013**, *49*, 1536−1538.

(12) Wang, Y.; Zhang, H. J.; Admar, A. S.; Luo, J.; Wong, C. C.; Borgna, A.; Lin, J. Improved Cyclability of Lithium-ion Battery Anode Using Encapsulated V_2O_3 Nanostructures in Well-Graphitized Carbon Fiber. *RSC Adv.* **2012**, *2*, 5748−5753.

(13) Pan, A.; Wu, H. B.; Yu, L.; Zhu, T.; Lou, X. W. (David) Synthesis of Hierarchical Three-Dimensional Vanadium Oxide Microstructures as High-Capacity Cathode Materials for Lithium-Ion Batteries. *ACS Appl. Mater. Interfaces* **2012**, *4*, 3874−3879.

(14) Mai, L.; Xu, L.; Han, C.; Xu, X.; Luo, Y.; Zhao, S.; Zhao, Y. Electrospun Ultralong Hierarchical Vanadium Oxide Nanowires with High Performance for Lithium Ion Batteries. *Nano Lett.* **2010**, *10*, 4750−4755.

(15) Xu, Y.; Zheng, L.; Wu, C.; Qi, F.; Xie, Y. New-Phased Metastable V_2O_3 Porous Urchinlike Micronanostructures: Facile Synthesis and Application in Aqueous Lithium Ion Batteries. *Chem.—Eur. J.* **2011**, *17*, 384−391.

(16) Li, H.; He, P.; Wang, Y.; Hosono, E.; Zhou, H. High-surface Vanadium Oxides with Large Capacities for Lithium-ion Batteries: from Hydrated Aerogel to Nanocrystalline $VO_2(B)$, V_6O_{13} and V_2O_5. *J. Mater. Chem.* **2011**, *21*, 10999−11009.

(17) Li, Y.; Li, J. Carbon-Coated Macroporous $Sn_2P_2O_7$ as Anode Materials for Li-Ion Battery. *J. Phys. Chem. C* **2008**, *112*, 14216−14219.

(18) Li, W.; Yang, J.; Wu, Z.; Wang, J.; Li, B.; Feng, S.; Deng, Y.; Zhang, F.; Zhao, D. A Versatile Kinetics-controlled Coating Method to Construct Uniform Porous TiO_2 Shells for Multifunctional Core-Shell Structures. *J. Am. Chem. Soc.* **2012**, *134*, 11864−11867.

(19) Li, G.; Tang, Z. Noble Metal Nanoparticle@Metal Oxide Core/Yolk-shell Nanostructures as Catalysts: Recent Progress and Perspective. *Nanoscale* **2014**, *6*, 3995−4011.

(20) Lauhon, L. J.; Gudiksen, M. S.; Wang, D.; Lieber, C. M. Epitaxial Core-shell and Core-multishell Nanowire Heterostructures. *Nature* **2002**, *420*, 57−61.

(21) Choi, S. H.; Kang, Y. C. Ultrafast Synthesis of Yolk-Shell and Cubic NiO Nanopowders and Application in Lithium Ion Batteries. *ACS Appl. Mater. Interfaces* **2014**, *6*, 2312−2316.

(22) Wang, F.; Deng, R.; Wang, J.; Wang, Q.; Han, Y.; Zhu, H.; Chen, X.; Liu, X. Tuning Upconversion through Energy Migration in Core-shell Nanoparticles. *Nat. Mater.* **2011**, *10*, 968−973.

(23) Chaudhuri, R. G.; Paria, S. Core/Shell Nanoparticles: Classes, Properties, Synthesis Mechanisms, Characterization, and Applications. *Chem. Rev.* **2012**, *112*, 2373−2433.

(24) Zhang, W. M.; Wu, X. L.; Hu, J. S.; Guo, Y. G.; Wan, L. J. Carbon Coated Fe_3O_4 Nanospindles as a Superior Anode Material for Lithium-Ion Batteries. *Adv. Funct. Mater.* **2008**, *18*, 3941−3946.

(25) Wu, Y.; Wen, Z.; Li, J. Hierarchical Carbon-Coated $LiFePO_4$ Nanoplate Microspheres with High Electrochemical Performance for Li-Ion Batteries. *Adv. Mater.* **2011**, *23*, 1126−1129.

(26) Yue, H.; Zhao, Y.; Ma, X.; Gong, J. Ethylene Glycol: Properties, Synthesis, and Applications. *Chem. Soc. Rev.* **2012**, *41*, 4218−4244.

(27) Firouzabadi, H.; Iranpoor, N.; Gholinejad, M.; Hoseini, J. Magnetite (Fe_3O_4) Nanoparticles-Catalyzed Sonogashira-Hagihara Reactions in Ethylene Glycol under Ligand-Free Conditions. *Adv. Synth. Catal.* **2011**, *353*, 125−132.

(28) Zhou, J.; Tian, G.; Chen, Y.; Meng, X.; Shi, Y.; Cao, X.; Pan, K.; Fu, H. In situ Controlled Growth of $ZnIn_2S_4$ Nanosheets on Reduced Graphene Oxide for Enhanced Photocatalytic Hydrogen Production Performance. *Chem. Commun.* **2013**, *49*, 2237−2239.

(29) Miao, X.; Pan, K.; Liao, Y.; Zhou, W.; Pan, Q.; Tian, G.; Wang, G. Controlled Synthesis of Mesoporous Anatase TiO_2 Microspheres as a Scattering Layer to Enhance the Photoelectrical Conversion Efficiency. *J. Mater. Chem. A* **2013**, *1*, 9853−9861.

(30) Tian, G.; Chen, Y.; Zhai, R.; Zhou, J.; Zhou, W.; Wang, R.; Pan, K.; Tian, C.; Fu, H. Hierarchical Flake-like Bi_2MoO_6/TiO_2 Bilayer Films for Visible-light-induced Self-cleaning Applications. *J. Mater. Chem. A* **2013**, *1*, 6961−6968.

(31) Qu, Y.; Zhou, W.; Ren, Z.; Du, S.; Meng, X.; Tian, G.; Pan, K.; Wang, G.; Fu, H. Facile Preparation of Porous $NiTiO_3$ Nanorods with Enhanced Visible-light-driven Photocatalytic Performance. *J. Mater. Chem.* **2012**, *22*, 16471−16476.

(32) Qu, Y.; Zhou, W.; Xie, Y.; Jiang, L.; Wang, J.; Tian, G.; Ren, Z.; Tian, G.; Fu, H. A Novel Phase-mixed $MgTiO_3$-$MgTi_2O_5$ Heterogeneous Nanorod for High Efficiency Photocatalytic Hydrogen Production. *Chem. Commun.* **2013**, *49*, 8510−8512.

(33) Pan, A. Q.; Wu, H. B.; Yu, L.; Lou, X. W. (David) Template-Free Synthesis of VO_2 Hollow Microspheres with Various Interiors and Their Conversion into V_2O_5 for Lithium-Ion Batteries. *Angew. Chem., Int. Ed.* **2013**, *52*, 2226−2230.

(34) Zhao, Y.; Jiang, L. Hollow Micro/Nanomaterials with Multilevel Interior Structures. *Adv. Mater.* **2009**, *21*, 3621−3638.

(35) Shen, L.; Yuan, C.; Luo, H.; Zhang, X.; Xu, K.; Xia, Y. Facile Synthesis of Hierarchically Porous $Li_4Ti_5O_{12}$ Microspheres for High Rate Lithium Ion Batteries. *J. Mater. Chem.* **2010**, *20*, 6998−7004.

(36) Wagner, C. D.; Riggs, W. M.; Davis, L. E.; Moulder, J. F. *Handbook of X-ray Photoelectrom Spectroscopy*; Perkin-Elmer Corporation: MN, 1979.

(37) Zhang, Y.; Fan, M.; Liu, X.; Huang, C.; Li, H. Beltlike V_2O_3@C Core-Shell-Structured Composite: Design, Preparation, Characterization, Phase Transition, and Improvement of Electrochemical Properties of V_2O_3. *Eur. J. Inorg. Chem.* **2012**, *10*, 1650−1659.

(38) Li, J.; Shen, B.; Hong, Z.; Lin, B.; Gao, B.; Chen, Y. A Facile Approach to Synthesize Novel Oxygen-doped g-C_3N_4 with Superior Visible-light Photoreactivity. *Chem. Commun.* **2012**, *48*, 12017−12019.

(39) Xiao, L.; Zhao, Y.; Yin, J.; Zhang, L. Clewlike ZnV_2O_4 Hollow Spheres: Nonaqueous Sol-Gel Synthesis, Formation Mechanism, and Lithium Storage Properties. *Chem.—Eur. J.* **2009**, *15*, 9442−9450.

(40) Zeng, L.; Zheng, C.; Xi, J.; Fei, H.; Wei, M. Composites of V_2O_3-ordered Mesoporous Carbon as Anode Materials for Lithium-ion Batteries. *Carbon* **2013**, *62*, 382−388.

(41) Shi, Y.; Wang, J.-Z.; Chou, S.-L.; Wexler, D.; Li, H.-J.; Ozawa, K.; Liu, H.-K.; Wu, Y.-P. Hollow Structured Li_3VO_4 Wrapped with Graphene Nanosheets in Situ Prepared by a One-Pot Template-Free Method as an Anode for Lithium-Ion Batteries. *Nano Lett.* **2013**, *13*, 4715−4720.